Vortex-Dominated Conical-Flow Computations Using Unstructured Adaptively-Refined Meshes

John T. Batina*
NASA Langley Research Center, Hampton, Virginia 23665

A conical Euler/Navier-Stokes algorithm is presented for the computation of vortex-dominated flows. The flow solver involves a multistage Runge-Kutta time-stepping scheme that uses a finite-volume spatial discretization on an unstructured grid made up of triangles. The algorithm also employs an adaptive mesh refinement procedure that enriches the mesh locally to resolve more accurately the vortical-flow features. Results are presented for several highly swept delta wing and circular cone cases at high angles of attack and at supersonic freestream flow conditions. Accurate solutions were obtained more efficiently when adaptive mesh refinement was used in contrast with refining the grid globally. The paper presents descriptions of the conical Euler/Navier-Stokes flow solver and adaptive mesh refinement procedures along with the results that demonstrate the capability.

Introduction

In recent years, the understanding and prediction of the complex flow about modern aircraft at high angles of attack have been research topics that have generated much interest within the computational fluid dynamics community.[1] These aircraft typically have sharp leading-edge wings or thin highly swept lifting surfaces such as delta wings that produce a vortical flow over the leeward side of the vehicle at high angles of attack. To predict such vortex-dominated flows, computer algorithms have been developed for the conical Euler and Navier-Stokes equations, as well as for the full three-dimensional equations. Newsome and Kandil,[1] for example, have reviewed the physical aspects and the numerical simulation of vortex-dominated flows. The primary emphasis of their discussion was on numerical methods that make use of vortex capturing using the Euler or Reynolds-averaged Navier-Stokes equations. In Ref. 1, these methods were surveyed and the future trends and challenges in the numerical simulation of vortical flows were identified.

Several researchers, such as Newsome and Thomas,[2] Kandil and Chuang,[3] and Chakravarthy and Ota,[4] have investigated the applicability of the Euler equations to vortex-dominated flows. It was found in Refs. 2–4 that inconsistent solutions may be obtained for round-edge delta wings depending on the grid density, the level of explicitly added artificial dissipation, or whether local or global time stepping was used. When these algorithm parameters were varied, both attached-flow and separated-flow solutions could be obtained for the same case. For sharp-edge delta wings, however, consistent solutions were always obtained irrespective of the grid density, artificial dissipation, or type of time stepping. This is because, for a sharp leading edge, the geometry determines where the flow will separate rather than the viscosity (either physical or numerical) of the flow. Therefore, the Euler equations are an appropriate equation set to model vortex-dominated flows about sharp-edge wings only. For these geometries, accurate solutions have been obtained in comparison with experimental data as reported by Murman and co-workers[5–7] and by Kandil et al.[8] It is recognized, however, that the Euler equations are not capable of predicting secondary flow features such as secondary vortices or effects due to Reynolds number.[2] For cases where these features are important, the Navier-Stokes equations are required to simulate the flow accurately. As an example, McMillin et al.[9] have shown that different types of leeside flow over highly swept sharp leading-edge delta wings at supersonic freestream conditions could be obtained using the Euler or Navier-Stokes methods.

Many of the vortex-dominated flow solutions that have been reported in the literature have been obtained without the grid resolution that is required for high accuracy. To improve the solution accuracy, much finer meshes are generally required. A globally fine mesh, however, is not practical since the calculations would require an enormous amount of computer resources. As an alternative, a zonal type of topology consisting of a locally fine mesh within a coarse global mesh is the approach that is needed to give accurate solutions while minimizing the computer costs. Recently, Fujii[10] reported the development of such a zonal method for solving the Navier-Stokes equations for both conical and three-dimensional flows. A three-dimensional zonal method has also been presented by Thomas and Krist.[11] In Refs. 10 and 11, the vortical-flow solutions were determined more accurately when an embedded fine mesh was used. The procedure requires that the user select a priori where the embedded fine mesh will be located, which requires some knowledge about the final solution. What is truly required is a solution adaptive mesh refinement procedure whereby the grid is enriched locally according to gradients of the instantaneous flowfield or to some measure of the quality of the solution. With this procedure, the user need not select where the grid should be refined since it is determined automatically by the adaptive mesh refinement procedures. Powell et al.,[12] for example, have reported the development of an adaptive mesh procedure for determining accurate solutions of the conical Euler equations. The main objective of the present investigation was to develop a similar procedure for accurately computing viscous as well as inviscid vortex-dominated conical flows. Therefore, the purpose of the paper is to present a new conical Euler/Navier-Stokes algorithm for the computation of vortex-dominated flows. The flow solver involves a multistage Runge-Kutta

Received June 23, 1989.

*Senior Research Scientist, Unsteady Aerodynamics Branch, Structural Dynamics Division. Senior Member AIAA.

time-stepping scheme that uses a finite-volume spatial discretization on an unstructured grid made up of triangles. The algorithm employs an adaptive mesh refinement procedure that enriches the mesh locally to resolve more accurately the vortical-flow features. Results are presented for several highly swept delta wing and circular cone cases at high angles of attack and at supersonic freestream conditions. The paper presents descriptions of the Euler/Navier-Stokes flow solver and adaptive mesh refinement procedures along with results that demonstrate the capability.

Governing Equations

The flow is governed by the time-dependent Navier-Stokes equations, which may be written in conservation law form as

$$\frac{\partial \boldsymbol{Q}}{\partial t}+\frac{\partial}{\partial x}(E-E_v)+\frac{\partial}{\partial y}(F-F_v)+\frac{\partial}{\partial z}(G-G_v)=0 \tag{1}$$

where $\boldsymbol{Q}$ is the vector of conserved variables defined by

$$\boldsymbol{Q}=[\rho,\rho u,\rho v,\rho w,e]^T \tag{2}$$

and E, F, and G are the convective or inviscid fluxes given by

$$E=\begin{bmatrix}\rho U\\ \rho Uu+p\\ \rho Uv\\ \rho Uw\\ (e+p)U+x_tp\end{bmatrix} \tag{3a}$$

$$F=\begin{bmatrix}\rho V\\ \rho Vu\\ \rho Vv+p\\ \rho Vw\\ (e+p)V+y_tp\end{bmatrix} \tag{3b}$$

$$G=\begin{bmatrix}\rho W\\ \rho Wu\\ \rho Wv\\ \rho Ww+p\\ (e+p)W+z_tp\end{bmatrix} \tag{3c}$$

The contravariant velocities U, V, and W are defined by

$$U=u-x_t,\qquad V=v-y_t,\qquad W=w-z_t \tag{4}$$

where x_t, y_t, and z_t are the grid speeds in the x, y, and z directions, respectively. The viscous fluxes are defined by

$$E_v=\begin{bmatrix}0\\ \tau_{xx}\\ \tau_{xy}\\ \tau_{xz}\\ b_x\end{bmatrix},\qquad F_v=\begin{bmatrix}0\\ \tau_{xy}\\ \tau_{yy}\\ \tau_{yz}\\ b_y\end{bmatrix},\qquad G_v=\begin{bmatrix}0\\ \tau_{xz}\\ \tau_{yz}\\ \tau_{zz}\\ b_z\end{bmatrix} \tag{5}$$

where τ_{xx}, τ_{xy}, τ_{xz}, . . ., are the viscous stresses, and b_x,b_y,b_z are given by

$$b_x=u\tau_{xx}+v\tau_{xy}+w\tau_{xz}-q_x \tag{6a}$$

$$b_y=u\tau_{xy}+v\tau_{yy}+w\tau_{yz}-q_y \tag{6b}$$

$$b_z=u\tau_{xz}+v\tau_{yz}+w\tau_{zz}-q_z \tag{6c}$$

where q_x, q_y, and q_z are the heat flux terms. Stokes hypothesis is assumed for bulk viscosity and the molecular viscosity is determined using Sutherland's law. The formulation presented herein is limited currently to laminar flows. The pressure p is determined by the equation of state for a perfect gas

$$p=(\gamma-1)[e-\tfrac{1}{2}\rho(u^2+v^2+w^2)] \tag{7}$$

and the equations have been nondimensionalized by the freestream density and the freestream speed of sound.

If interest is restricted to supersonic flow past conical bodies, then the conical-flow assumption can be made. This reduces the problem from three dimensions to two dimensions, which significantly decreases the computational resources that are required to investigate such flows. The conical-flow assumption is exact for inviscid supersonic flow. For viscous flow, however, a length dependence remains in the Reynolds number Re, although the flow may be considered to be locally conical. The Reynolds number, therefore, determines the location of the plane at which the solution is determined. The conical-flow assumption involves a change of variables according to

$$\xi=x,\qquad \eta=y/x,\qquad \zeta=z/x \tag{8}$$

The three-dimensional Navier-Stokes equations then reduce to

$$\frac{\partial \boldsymbol{Q}}{\partial t}+\frac{\partial}{\partial \eta}(\hat{F}-\eta\hat{E})+\frac{\partial}{\partial \zeta}(\hat{G}-\zeta\hat{E})+2\hat{E}=0 \tag{9}$$

where

$$\hat{E}=E-E_v,\qquad \hat{F}=F-F_v,\qquad \hat{G}=G-G_v \tag{10}$$

If interest is restricted to inviscid flow, the viscous fluxes are simply set equal to zero, which yields the conical Euler equations. Equation (9) may be rewritten in integral form for solution as

$$\frac{\partial}{\partial t}\int_\Omega \boldsymbol{Q}\,d\eta\,d\zeta+\int_{\partial\Omega}[(\hat{F}-\eta\hat{E})\,d\zeta-(\hat{G}-\zeta\hat{E})\,d\eta]+\int_\Omega 2\hat{E}=0 \tag{11}$$

where the second integral is a boundary integral resulting from application of the divergence theorem.

Solution Algorithm

Spatial Discretization

The Euler/Navier-Stokes equations in integral form are solved using a finite-volume algorithm developed for analysis with an unstructured grid made up of triangles. The algorithm is a nodal scheme whereby the flow variables are stored at the vertices of the triangles. The control volume is taken to be the neighboring triangles that have a vertex at that node. The boundary integral in Eq. (11) is approximated as follows. Along each edge of the control volume boundary the inviscid fluxes at the two endpoints are averaged. The contribution to the boundary integral is determined by taking the product of the averaged fluxes with the directed length of the edge. The contribution due to the viscous fluxes is computed differently. This is because the viscous fluxes contain normal and shear stresses that involve the spatial derivatives of the velocity components. These derivatives are computed for each triangle first, using formulas such as

$$\frac{\partial u}{\partial \eta}=\frac{1}{A}\left[\frac{u_1+u_2}{2}(\zeta_2-\zeta_1)+\frac{u_2+u_3}{2}(\zeta_3-\zeta_2)+\frac{u_3+u_1}{2}(\zeta_1-\zeta_3)\right] \tag{12}$$

where the nodes of the triangle in this example are numbered 1, 2, 3, and A is the area of the triangle. The viscous fluxes

are then averaged along each edge of the control volume boundary, using the values from the two triangles that share the respective edge. The contribution to the boundary integral is determined finally by taking the product of the averaged viscous fluxes with the directed length of the edge. This treatment of the inviscid and viscous flux terms reduces conceptually to central differencing on a rectangular mesh. Thus, the algorithm of the present study may be regarded as a central-difference-type flow solver.

Artificial Dissipation

The unsteady Navier-Stokes equations are nondissipative outside of the boundary layer, and, therefore, the numerical solution requires some form of artificial dissipation to prevent oscillations near shock waves and to damp high-frequency uncoupled error modes. On structured meshes using central-difference-type flow solvers, an adaptive blend of second and fourth differences of the conserved variables has been shown to be an effective form of dissipation. In the present unstructured mesh flow solver, a blend of harmonic and biharmonic operators is employed, corresponding to second and fourth differences, respectively. The biharmonic operator provides a background dissipation to damp high-frequency errors, and the harmonic operator prevents oscillations near shocks. The harmonic operator is multiplied by a pressure switch that is first-order accurate near shocks and is second-order accurate in smooth regions of the flow. The biharmonic operator is third-order accurate and is adaptively turned off to prevent overshoots in regions of shock waves.

Time Integration

The Euler/Navier-Stokes equations are integrated in time using a four-stage Runge-Kutta time-stepping scheme. In this scheme, the artificial dissipation is evaluated only at the first stage for computational efficiency. Also, when solving the Navier-Stokes equations, the viscous fluxes are evaluated only at the first stage for further computational efficiency. This effectively reduces the computational work that is required to evaluate the viscous fluxes by a factor of 4.

Implicit Residual Smoothing

The explicit time-integration scheme described in the previous section has a step size that is limited by the Courant-Friedricks-Lewy (CFL) condition. To acclerate convergence to steady state, the CFL condition may be relaxed by averaging the residual with values at neighboring grid points. This is accomplished by replacing the residual R_i by the smoothed residual $\bar{R}_i$ given by

$$\bar{R}_i - \varepsilon \nabla^2 \bar{R}_i = R_i \tag{13}$$

where ε is a constant that controls the amount of smoothing and ∇^2 is an undivided Laplacian operator. These implicit equations are solved approximately using several Jacobi iterations.

Convergence to steady state is accelerated further using local time stepping, which uses the maximum allowable step size at each grid point as determined by a local stability analysis. For unsteady applications, however, a global time step must be used because of the time-accuracy requirement. The maximum allowable global time step may be increased to a value that is larger than that dictated by the CFL condition by using a time-accurate version of Eq. (13) similar to that derived in Ref. 13. In this procedure, the constant ε is replaced by a parameter that varies from grid point to grid point and is defined by

$$\varepsilon = \max\left[\frac{1}{4}\left(\frac{\Delta t^2}{\Delta t_{\mathrm{CFL}}^2} - 1\right), 0.0\right] \tag{14}$$

In Eq. (14), Δt is the time step taken, and Δt_{CFL} is the locally allowable time step for the four-stage Runge-Kutta time-stepping scheme.

Boundary Conditions

For viscous flow computations, the no-slip surface boundary condition is imposed by setting the three velocity components equal to zero at grid points that lie on the surface of the body. For inviscid-flow computations, the governing equations are first rewritten in terms of the flux velocity q where

$$q = (v - \eta u - \eta_t)\Delta\zeta - (w - \zeta u - \zeta_t)\Delta\eta \tag{15}$$

To satisfy the flow tangency (or slip) boundary condition, the flux velocity is simply set equal to zero at grid points that lie on the surface of the body. In the far field, freestream boundary conditions are imposed for simplicity and a reasonably large computational grid is used so that the bow shock is captured as a part of the solution.

Grid Generation

In the present study, the grids (before adaptive mesh refinement) were generated analytically by using a modified Joukowski transformation, which is similar to that used to create meshes with quadrilateral cells.[3,12] The procedure was generalized to create meshes with triangular cells to generate the necessary input to the flow solver. The required input includes a list of nodes and a list of "connectivity," that is, for each triangle, the three nodes that make up the triangle.

Adaptive Refinement Procedure

An adaptive refinement procedure was developed to enrich the mesh in regions of high flow gradients to resolve more accurately certain features of the flow. In the present study, total pressure loss was used as an indicator to determine where to refine the mesh because total pressure losses are a good indicator of the vortical-flow structure.[14] In this procedure, the total pressure loss is computed at each node in the mesh. Along each edge of each triangle, the total pressure losses at the two endpoints are averaged and then compared with a predetermined tolerance. If the tolerance is exceeded, a new node is created at the midpoint of the edge and the triangle is divided. Each time the mesh is refined, a triangle may be divided in one of two ways. A triangle is divided into four smaller triangles if two or more of the edges that make up the triangle have average total pressure losses that exceed the preset tolerance. If only one edge exceeds this tolerance, then the triangle is divided into two elements by bisecting that edge. The coordinates of the new node are determined consequently by averaging the coordinates of the endpoints that make up the bisected edge. Special care must be taken, however, when an edge that is to be divided lies on an inner boundary of the grid because the midpoint of the edge does not generally lie on the boundary. In this case, the location of the new node is determined generally by using a spline of the boundary coordinates. For the simple geometries considered in the present study, however, the location of the new node on the boundary is determined exactly since the geometry is defined analytically.

Results and Discussion

To demonstrate the Euler/Navier-Stokes flow solver and the adaptive mesh refinement procedures, calculations were performed for several highly swept delta wing and circular cone cases at high angles of attack and at supersonic freestream flow conditions. In these calculations, five cases were considered, as listed in Table 1. The first three cases involve a 75-deg swept flat-plate delta wing at a freestream Mach number of $M_\infty = 1.4$, and the calculations were performed using the conical Euler equations. The first case, hereafter referred to as case 1, has an angle of attack of $\alpha = 20$ deg. The second case, referred to as case 2, has an

Table 1 Summary of vortex-dominated conical flow cases

Case	Geometry	M_∞	α, deg	β, deg	Φ, deg	Re	Flow equations
1	75-deg swept flat-plate delta wing	1.4	20	0	0	∞	Conical Euler
2	75-deg swept flat-plate delta wing	1.4	20	10	0	∞	Conical Euler
3	75-deg swept flat-plate delta wing	1.4	20	0	30	∞	Conical Euler
4	70-deg swept elliptic cone delta wing	2.0	10	0	0	0.5×10^6	Conical Navier-Stokes
5	85-deg swept circular cone	1.4	20	0	0	0.5×10^6	Conical Navier-Stokes

angle of attack of 20 deg and a yaw angle of $\beta = 10$ deg. The third case, referred to as case 3, has the same freestream flow conditions as case 1, but the wing was forced to oscillate in a harmonic rolling motion with an amplitude of $\Phi = 30$ deg and a reduced frequency of $k = 0.3$ (based on one-half of the distance from the wing apex and the streamwise freestream speed). The last two cases involve highly swept elliptic and circular cones, and the calculations were performed using the conical Navier-Stokes equations. The fourth case, referred to as case 4, involves a thin elliptic cone that corresponds to a delta wing that is swept 70 deg along the leading edge with a thickness ratio of 14:1. The freestream flow conditions for case 4 were $M_\infty = 2.0$, $\alpha = 10$ deg, and $Re = 0.5 \times 10^6$. The last case, referred to as case 5, involves an 85-deg swept circular cone at $M_\infty = 1.4$, $\alpha = 20$ deg, and $Re = 0.5 \times 10^6$.

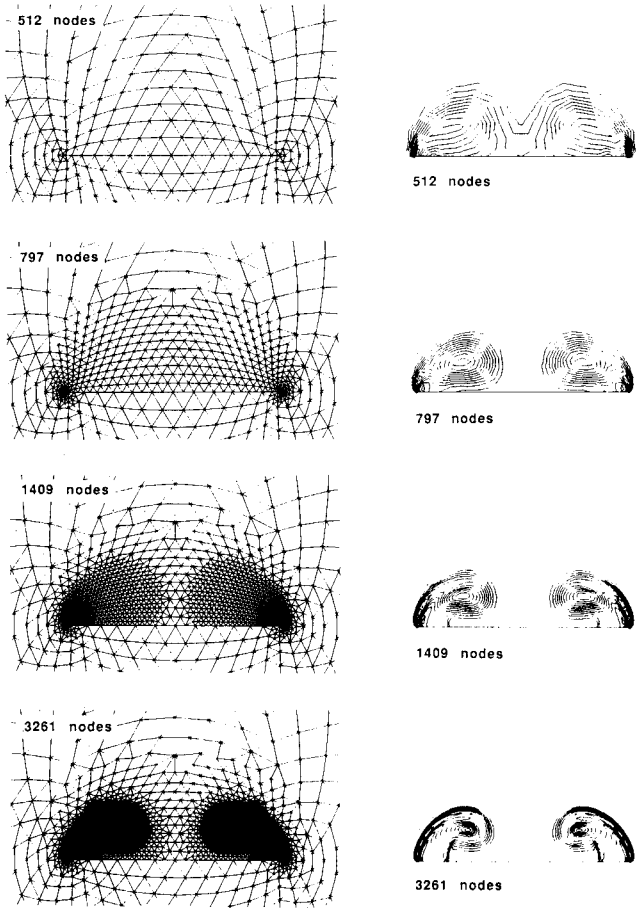

Fig. 1 Effects of adaptive mesh refinement on the total pressure loss contours for a 75-deg swept flat-plate delta wing at $M_\infty = 1.4$ and $\alpha = 20$ deg, computed using the conical Euler equations.

Case 1

Case 1 was selected to test the adaptive mesh refinement procedures for a flat-plate delta wing using the conical Euler equations by making comparisons with similar results reported in Ref. 12. The mesh that was used to start the calculation has 32 nodes around the wing and 16 nodes in the outward direction for a total of 512 nodes. A partial view of the mesh is shown in the upper left part of Fig. 1. Results for case 1 were obtained using adaptive mesh refinement by starting with the coarse mesh containing 512 nodes and adapting to the total pressure losses of the instantaneous solutions to determine a locally fine mesh. The flow solver was run for a total of 4000 iterations and the mesh was adapted at iterations 500, 1000, and 1500. Adapting the mesh every 500 iterations produces intermediate results that are converged to plotting accuracy; although this is not a requirement for the adaptation procedure to be numerically stable or to produce accurate final results.

A summary of the meshes and the corresponding total pressure loss contours for case 1 is shown in Fig. 1. The total pressure loss contours obtained from the 32×16 mesh (512 nodes) solution indicate that large vortices are produced on the leeward side of the wing due to the separated flow from the leading edges. These vortices are very diffuse due to the coarseness of the mesh (and subsequent large artificial dissipation in the solution), and no crossflow shock waves are apparent. Adapting the mesh to this solution results in an increase in the total number of grid points to 797 nodes. Use of this mesh produces a flow with more clearly defined vortices. Adapting the mesh a second time to the instantaneous flow solution produces a grid with 1409 nodes. With this mesh, crossflow shock waves become visible in the solution beneath each of the vortices. Adapting the mesh a third time produces the final mesh, which contains a total of 3261 nodes. The final solution obtained on this mesh clearly shows that the flow separates from each of the leading edges producing large circular vortices and that the crossflow shock waves beneath the vortices are now sharply captured. A solution of comparable accuracy on a globally fine mesh would requre 32,768 nodes (256×128). A spatially accurate solution is thus obtained for this case with adaptive mesh refinement, using an order of magnitude fewer grid points (3261 nodes).

Figure 2 shows a comparison of total pressure loss contours from the final solution of Fig. 1 with similar results presented in Ref. 12. An expanded view of the total pressure loss contours describing the right leading-edge vortex from Fig. 1 are shown in Fig. 2a; the contours from Ref. 12 are shown in Fig. 2b. Comparison of the two sets of contours indicates good agreement, which tends to verify the adaptive mesh refinement capability of the present study for determining accurate solutions of the conical Euler equations.

Case 2

Case 2 was selected to demonstrate application of the adaptive mesh refinement procedures to a wing that is yawed.

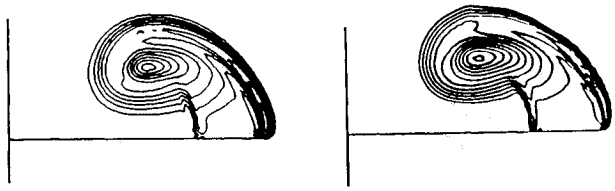

a) Contours of present study b) Contours of Ref. 12

Fig. 2 Comparison of total pressure loss contours for a 75-deg swept flat-plate delta wing at $M_\infty = 1.4$ and $\alpha = 20$ deg, computed using the conical Euler equations.

Similar to case 1, the calculations were performed by starting with the coarse 32 × 16 mesh and adaptively refining the mesh three times. The flow solver was run for a total of 4000 iterations and the mesh was adapted at iterations 500, 1000, and 1500. A summary of the meshes and the corresponding total pressure loss contours for case 2 is shown in Fig. 3. For this case there is a strong flat vortex produced by the separated flow from the windward (left) leading edge with a crossflow shock wave beneath the vortex. There is also a weaker, more circular vortex produced by the separated flow from the leeward (right) leading edge. With the coarse grids containing 512 (original mesh) and 807 (one enrichment) nodes, the shock wave beneath the windward vortex is not detected in the total pressure loss contours. Upon further enrichment to a grid containing 1363 nodes, the shock begins to appear, and with the final grid of 2801 nodes the shock is shown to be sharply captured. The total pressure loss contours of Fig. 3 indicate that the vortical-flow features are defined more clearly when the mesh is adaptively refined. An accurate solution is thus obtained more efficiently when using adaptive mesh refinement in contrast with refining the grid globally.

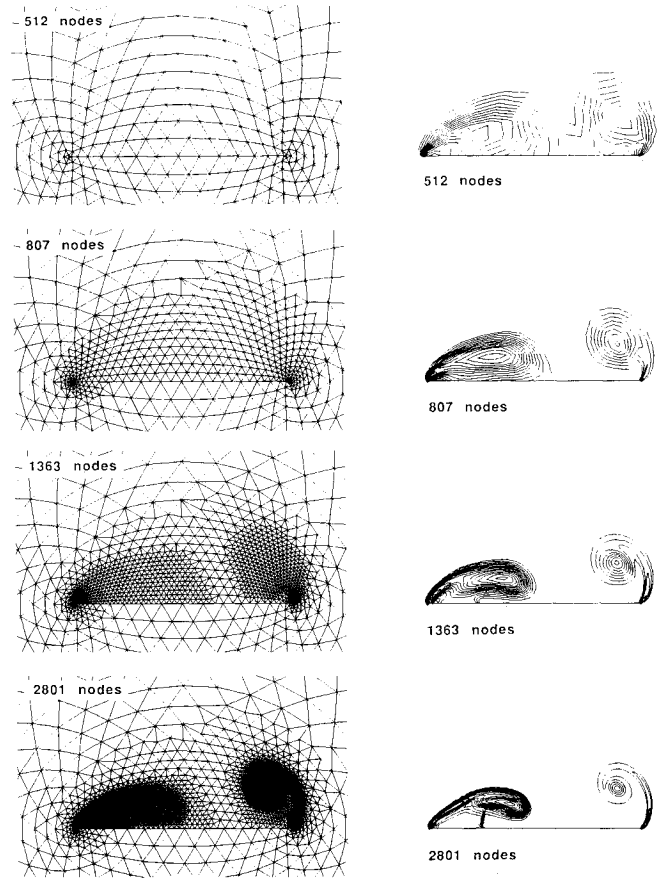

Fig. 3 Effects of adaptive mesh refinement on the total pressure loss contours for a 75-deg swept flat-plate delta wing at $M_\infty = 1.4$, $\alpha = 20$ deg, and $\beta = 10$ deg, computed using the conical Euler equations.

Case 3

Case 3 was selected to demonstrate the time-accurate capability of the conical Euler flow solver, although the results are actually only locally conical. The unsteady results were obtained for the rolling delta wing oscillating harmonically with an amplitude of 30 deg at $k = 0.3$ using 2400 steps per cycle of motion. In these calculations, the grid was first adapted to the steady solution to create a fine embedded mesh locally, which was then used in the unsteady calculation. The fine embedded region was made large enough so that the moving vortices and shock waves were always contained within this region and the total grid contained 5152 nodes. It is recognized, however, that, for unsteady applications, a de-refinement procedure can be used in addition to the refinement procedure to remove as well as to add nodes and elements during the calculation. Also during the unsteady calculation, the grid was moved as a rigid body to conform to the instantaneous position of the wing. Three cycles of motion were computed to obtain a periodic solution. Instantaneous total pressure loss contours at eight points in time during the third cycle of motion are shown in Fig. 4. In each part of the figure, the instantaneous angular position in the cycle $k\tau$ is noted where τ is time normalized by one-half of the reference length and the streamwise freestream speed.

During the first half of the cycle as the wing rolls clockwise to the maximum amplitude and then back to straight and level, the crossflow shock wave beneath the left vortex disappears, the left vortex weakens, and the right vortex grows in strength. During the second half of the cycle, the opposite situation occurs; the shock wave beneath the right vortex disappears, the right vortex weakens, and the left vortex grows in strength. It is easy to see that the solution is periodic in the third cycle of motion by comparing the total pressure loss contours at any two points in time that are 180 deg out of phase in the cycle. The two sets of total pressure loss contours, 180 deg out of phase, are antisymmetric as shown in Fig. 4.

Figure 5 show the normal force and rolling moment coefficients vs the instantaneous roll angle during the third cycle of motion. The normal force coefficient is shown in Fig. 5a, and the rolling moment coefficient is shown in Fig. 5b. In these results, the roll angle ϕ is defined as positive clockwise, the normal force is positive up, and the rolling moment is positive clockwise. Both coefficients have been normalized by the wing span. Figure 5a indicates that the normal force is at a minimum value at both the positive and negative extremes of the rolling motion. This occurs because the flow is antisymmetric at these two points in time and, thus the normal force response has twice the frequency of the excitation. Figure 5b indicates that the rolling moment has a small stable damping and the same frequency as the excitation.

Case 4

Results were first obtained for case 4 without adaptive mesh refinement to test the Navier-Stokes flow solver by making comparisons with the results of Ref. 15. As discussed earlier, the Navier-Stokes results are only locally conical because of the length dependence in the Reynolds number. The mesh that was used in these computations is shown in Fig. 6. It has 256 points around the body and 64 points in the outward direction for a total of 16,384 nodes. The mesh was generated with the same grid program that produced the original flat-plate delta wing grid of cases 1–3, except that the outward stretching was modified to cluster points near the body to resolve the boundary layer. Calculations were performed for 2500 iterations, which reduced the L_2 norm of the density residual by over four orders of magnitude. The resulting crossflow velocity vectors are shown in Fig. 7. These

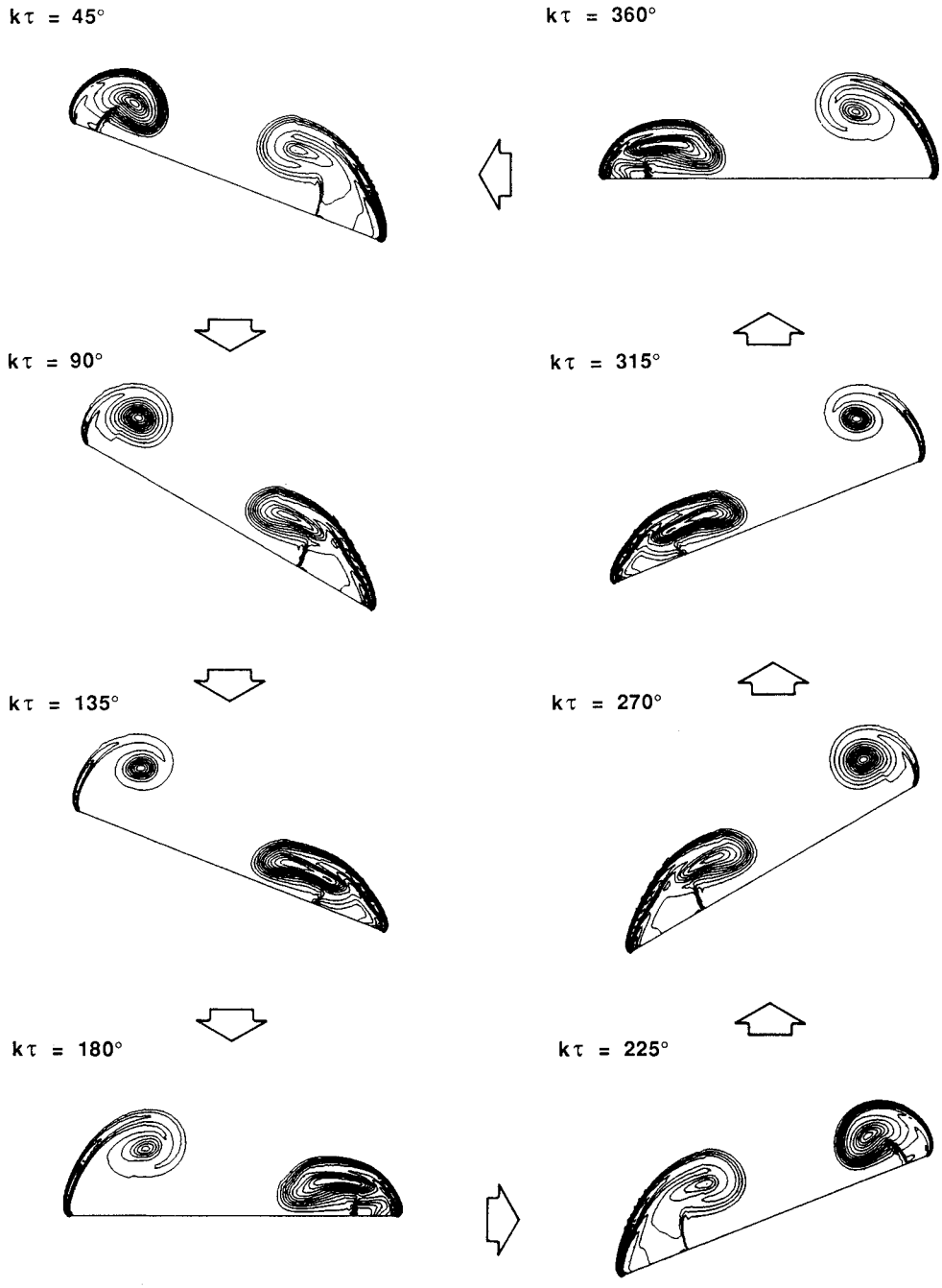

Fig. 4 Instantaneous total pressure loss contours during a cycle of harmonic rolling for a 75-deg swept flat-plate delta wing at $M_\infty = 1.4$, $\alpha = 20$ deg, $\beta = 0$ deg, $\Phi = 30$ deg, and $k = 0.3$, computed using the conical Euler equations.

velocity vectors indicate that the flow separates near the rounded leading edge and then forms a large primary vortex on the leeward side of the wing. The induced flow beneath the vortex produces an adverse pressure gradient that causes the boundary layer to separate and form a second weaker vortex outboard of the primary vortex. Close examination of the velocity vectors of Fig. 7 reveals that additional vortices are also present in the flow. It is recognized, however, that, for the Reynolds number considered here ($Re = 0.5 \times 10^6$), these additional vortices calculated for laminar flow may disappear with the inclusion of turbulence modeling in the analysis.

Figure 8 shows the corresponding pressure coefficient distribution on the surface of the wing. The pressures show an increase in suction on the leeward side from approximately $y/y_{le} = 0.45$ to the leading edge due to the presence of the strong primary vortex. The weaker, secondary vortex produces a small suction peak in the pressure distribution near $y/y_{le} = 0.7$. The pressure distribution is in close agreement with that of Thomas and Newsome,[15] who reported Navier-Stokes results for case 4, obtained using a method based on upwind differencing for the pressure and convective terms (inviscid fluxes) and central differencing for the shear stress and heat flux terms (viscous fluxes). The good agreement between the two sets of results tends to verify the Navier-Stokes flow solver of the present study. Small differences between the results are attributed to differences in grids as well as to differences between the two methods.

Calculations were then repeated for case 4 using adaptive mesh refinement to test the enrichment procedures for a viscous-flow application. Results were obtained by starting with a relatively coarse mesh (128×32) containing 4096 nodes, a partial view of which is shown in the upper left part of Fig. 9. The flow solver was run for a total of 4000 iterations and the mesh was adapted at iterations 1000 and 2000. A summary of the meshes and the corresponding total pressure loss contours for case 4 is shown in Fig. 9. With the

coarse grid of 4096 nodes, the total pressure loss contours indicate that the large primary vortex is very diffuse and that the boundary layer appears to be thick. The mesh was then adapted twice to the total pressure losses of the instantaneous solution, which enriched the mesh locally on the leeside of the wing to resolve more accurately the vortical flow, and close to the wing to better resolve the boundary layer. This resulted in meshes containing 7048 and 15,689 nodes. When the mesh is successively refined, the primary vortex becomes smaller, the secondary vortical-flow features become clearly defined, and the boundary layer is much thinner around the wing in comparison with the coarse grid results. A solution of comparable accuracy on a globally fine mesh would require 65,536 nodes (512 × 128). In comparison with the results of Fig. 7, the primary vortex is smaller and has moved outboard when the mesh is refined. This consequently shifts the increase in suction pressure on the leeward side of the wing outboard, as shown in Fig. 10. Also, since the secondary and tertiary vortices are defined more clearly in the adapted solution, the small suction peaks in the pressure distribution are larger, as indicated further in Fig. 10.

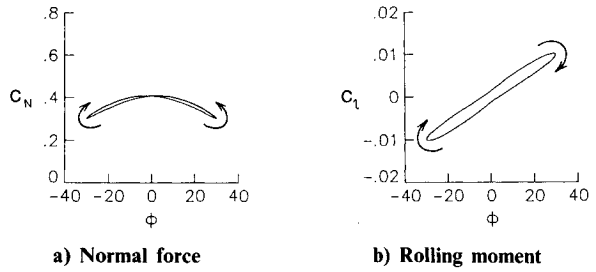

a) Normal force b) Rolling moment

Fig. 5 Coefficients vs instantaneous roll angle for a 75-deg swept flat-plate delta wing at $M_\infty = 1.4$, $\alpha = 20$ deg, $\beta = 0$ deg, $\Phi = 30$ deg, and $k = 0.3$, computed using the conical Euler equations.

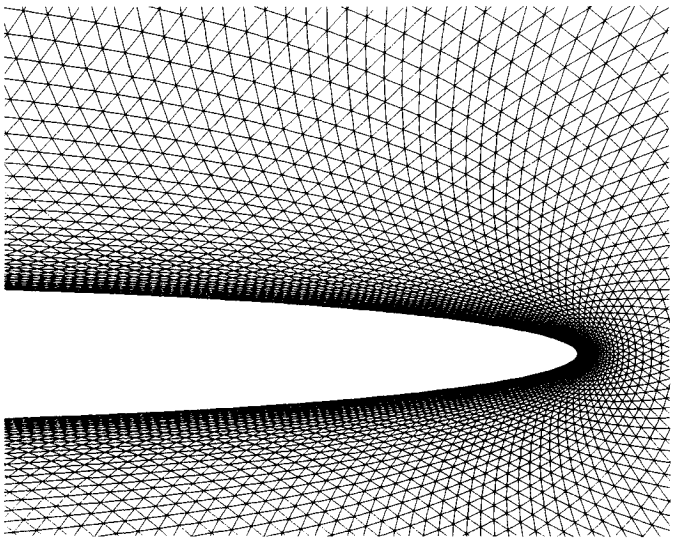

Fig. 6 Mesh of triangles (256 × 64) for a 70-deg swept elliptic cone delta wing.

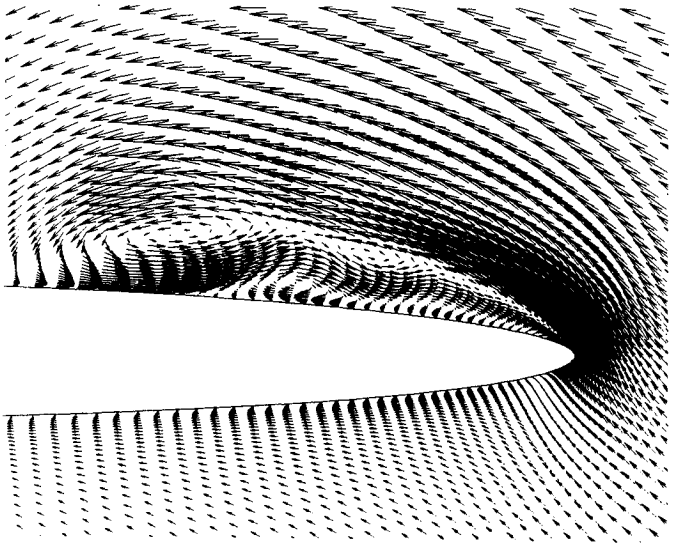

Fig. 7 Crossflow velocity vectors for a 70-deg swept elliptic cone delta wing at $M_\infty = 2.0$, $\alpha = 10$ deg, and $Re = 0.5 \times 10^6$, computed using the conical Navier-Stokes equations.

Case 5

Case 5 was selected to demonstrate further the adaptive mesh refinement procedures for a viscous flow about a circular cone. The calculations were performed by starting with a coarse 64 × 32 mesh (2048 nodes) and adaptively refining the mesh twice. The flow solver was run for a total of 4000 iterations and the mesh was adapted at iterations 1000 and 2000. A summary of the meshes and the corresponding total

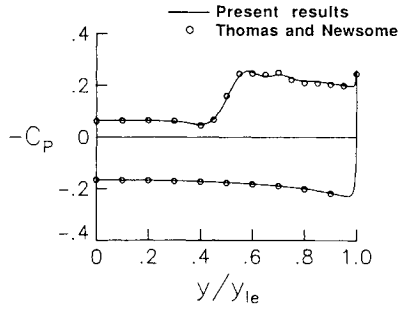

Fig. 8 Comparisons of crossflow pressure coefficient distributions on a 70-deg swept elliptic cone delta wing at $M_\infty = 2.0$, $\alpha = 10$ deg, and $Re = 0.5 \times 10^6$, computed using the conical Navier-Stokes equations.

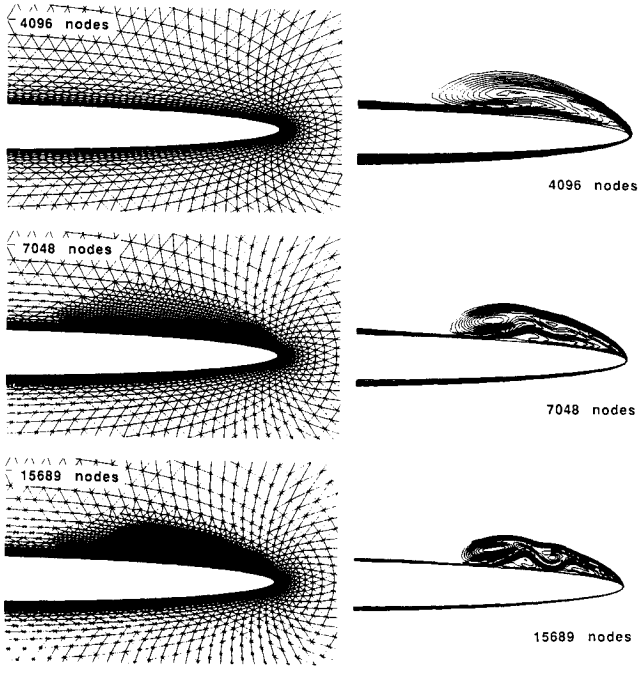

Fig. 9 Effects of adaptive mesh refinement on the total pressure loss contours for a 70-deg swept elliptic cone delta wing at $M_\infty = 2.0$, $\alpha = 10$ deg, and $Re = 0.5 \times 10^6$, computed using the conical Navier-Stokes equations.

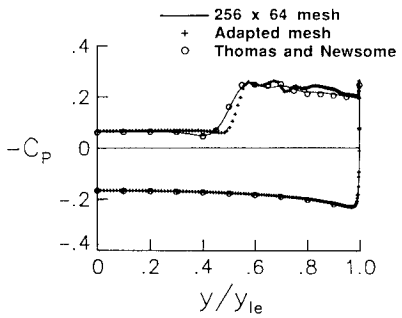

Fig. 10 Further comparisons of crossflow pressure coefficient distributions on a 70-deg swept elliptic cone delta wing at $M_\infty = 2.0$, $\alpha = 10$ deg, and $Re = 0.5 \times 10^6$, computed using the conical Navier-Stokes equations.

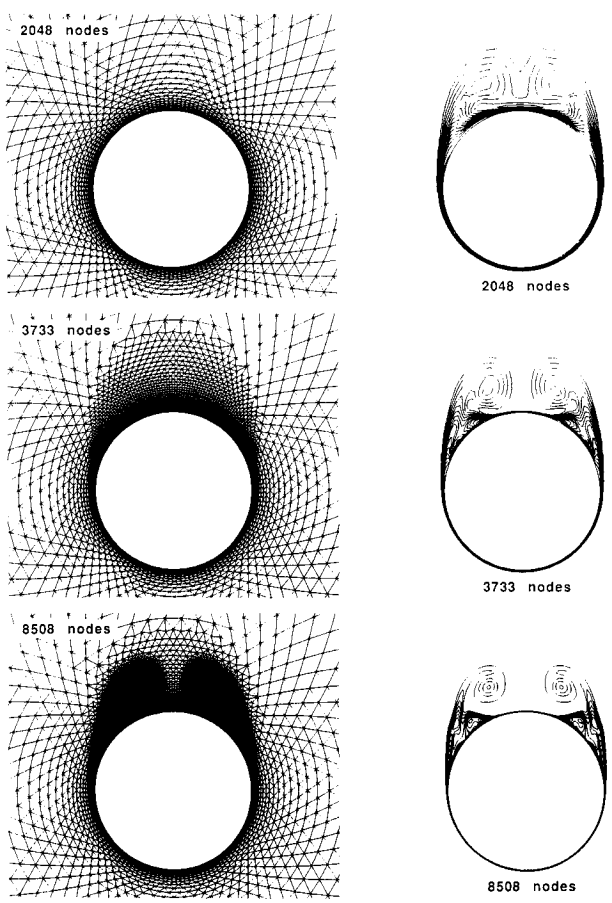

Fig. 11 Effects of adaptive mesh refinement on the total pressure loss contours for an 85-deg swept circular cone at $M_\infty = 1.4$, $\alpha = 20$ deg, and $Re = 0.5 \times 10^6$, computed using the conical Navier-Stokes equations.

pressure loss contours for case 5 is shown in Fig. 11. For this case, there are two large, symmetric, primary vortices that are produced by the separated flow from the left and right sides of the cone. With the coarse mesh containing 2048 nodes, the primary vortices are very diffuse, the secondary vortical-flow features are absent, and the boundary layer appears thick. When the grid is refined to 3733 nodes and then to 8508 nodes, the primary vortices become smaller and more sharply defined, secondary and tertiary vortices become apparent in the flow, and the boundary layer appears to be much thinner in comparison with the coarse grid results. An accurate solution is thus obtained for this case with adaptive mesh refinement, using a factor of approximately four fewer grid points (8508 nodes) in comparison with a globally fine mesh (32,768 nodes).

Concluding Remarks

A conical Euler/Navier-Stokes algorithm was presented for the computation of vortex-dominated flows. The flow solver involves a multistage Runge-Kutta time-stepping scheme that uses a finite-volume spatial discretization on an unstructured grid made up of triangles. The algorithm employs an adaptive mesh refinement procedure that enriches the mesh locally to resolve more accurately the vortical-flow features. Results were presented for several highly swept delta wing and circular cone cases at high angles of attack and at supersonic freestream flow conditions. Results for these cases demonstrated the ability to predict accurately complex vortex-dominated flows. Accurate solutions were obtained more efficiently when adaptive mesh refinement was used in contrast with refining the grid globally.

References

[1]Newsome, R. W., and Kandil, O. A., "Vortical Flow Aerodynamics—Physical Aspects and Numerical Simulations," AIAA Paper 87-0205, Jan. 1987.

[2]Newsome, R. W., and Thomas, J. L., "Computation of Leading-Edge Vortex Flows," *Proceedings of the Conference on Vortical Flow Aerodynamics*, NASA Langley Research Center, Hampton, VA, Oct. 1985.

[3]Kandil, O. A., and Chuang, A., "Influence of Numerical Dissipation in Computing Supersonic Vortex-Dominated Flows," AIAA Paper 86-1073, May 1986.

[4]Chakravarthy, S. R., and Ota, D. K., "Numerical Issues in Computing Inviscid Supersonic Flow Over Conical Delta Wings," AIAA Paper 86-0440, Jan. 1986.

[5]Murman, E. M., Powell, K. G., Miller, D. S., and Wood, R. M., "Comparisons of Computations and Experimental Data for Leading Edge Vortices—Effects of Yaw and Vortex Flaps," AIAA Paper 86-0439, Jan. 1986.

[6]Powell, K. G., Murman, E. M., Wood, R. M., and Miller, D. S., "Comparison of Experimental and Numerical Results for Delta Wings with Vortex Flaps," *Journal of Aircraft*, Vol. 25, No. 5, 1988, pp. 405–412.

[7]Murman, E. M., and Rizzi, A., "Applications of Euler Equations to Sharp Edge Delta Wings With Leading Edge Vortices," AGARD-CP-412, Nov. 1986.

[8]Kandil, O. A., Chuang, A. H., and Shifflette, J. M., "Finite-Volume Euler and Navier-Stokes Solvers for Three-Dimensional and Conical Vortex Flows Over Delta Wings," AIAA Paper 87-0041, Jan. 1987.

[9]McMillin, S. N., Thomas, J. L., and Murman, E. M., "Euler and Navier-Stokes Solutions for the Leeside Flow Over Delta Wings at Supersonic Speeds," AIAA Paper 87-2270, July 1987.

[10]Fujii, K., "A Method to Increase the Accuracy of Vortical Flow Simulations," AIAA Paper 88-2562, July 1988.

[11]Thomas, J. L., and Krist, S., "An Embedded Grid Formulation Applied to Delta Wings," Presented at the NASA Computational Fluid Dynamics Conference, Moffett Field, CA, March 1989.

[12]Powell, K. G., Beer, M. A., and Law, G. L., "An Adaptive Embedded Mesh Procedure for Leading-Edge Vortex Flows," AIAA Paper 89-0080, Jan. 1989.

[13]Venkatakrishnan, V., "Computation of Unsteady Transonic Flows over Moving Airfoils," Ph.D. Dissertation, Princeton University, Princeton, NJ, 1986.

[14]Powell, K. G., Murman, E. M., Perez, E. S., and Baron, J. R., "Total Pressure Loss in Vortical Solutions of the Conical Euler Equations," *AIAA Journal*, Vol. 25, No. 3, 1987, pp. 360–368.

[15]Thomas, J. L., and Newsome, R. W., "Navier-Stokes Computations of Lee-Side Flows Over Delta Wings," AIAA Paper 86-1049, May 1986.